Monthly Notices
of the
ROYAL ASTRONOMICAL SOCIETY

MNRAS **456,** 4145–4155 (2016) doi:10.1093/mnras/stv2490

The outburst decay of the low magnetic field magnetar SWIFT J1822.3−1606: phase-resolved analysis and evidence for a variable cyclotron feature

Guillermo A. Rodríguez Castillo,[1,2]⋆ Gian Luca Israel,[1] Andrea Tiengo,[3,4,5] David Salvetti,[3] Roberto Turolla,[6,7] Silvia Zane,[7] Nanda Rea,[8,9] Paolo Esposito,[3,10] Sandro Mereghetti,[3] Rosalba Perna,[11] Luigi Stella,[1] José A. Pons,[12] Sergio Campana,[13] Diego Götz[14] and Sara Motta[15]

[1]*INAF – Osservatorio Astronomico di Roma, Via Frascati 33, I-00040 Monte Porzio Catone, Italy*
[2]*Dipartimento di Fisica, Sapienza Università di Roma, Piazzale Aldo Moro 5, I-00185 Rome, Italy*
[3]*INAF – IASF Milano, Via E. Bassini 15, I-20133 Milano, Italy*
[4]*Istituto Universitario di Studi Superiori, Piazza della Vittoria 15, I-27100 Pavia, Italy*
[5]*Istituto Nazionale di Fisica Nucleare, Sezione di Pavia, Via A. Bassi 6, I-27100 Pavia, Italy*
[6]*Dipartimento di Fisica e Astronomia, Università di Padova, Via Marzolo 8, I-35131 Padova, Italy*
[7]*Mullard Space Science Laboratory, University College London, Holmbury St. Mary, Dorking, Surrey RH5 6NT, UK*
[8]*Astronomical Institute 'Anton Pannekoek', University of Amsterdam, Postbus 94249, NL-1090 GE Amsterdam, the Netherlands*
[9]*Institute of Space Sciences (CSIC-IEEC), Campus UAB, Carrer de Can Magrans, s/n, E-08193 Barcelona, Spain*
[10]*Harvard–Smithsonian Center for Astrophysics, 60 Garden Street, Cambridge, MA 02138, USA*
[11]*Department of Physics and Astronomy, Stony Brook University, Stony Brook, NY 11794, USA*
[12]*Departament de Física Aplicada, Universitat d'Alacant, Ap. Correus 99, E-03080 Alacant, Spain*
[13]*INAF – Osservatorio Astronomico di Brera, Via E. Bianchi 46, I-23807 Merate, Italy*
[14]*AIM (CEA/DSM-CNRS-Université Paris Diderot), Irfu/Service d'Astrophysique, Saclay, F-91191 Gif-sur-Yvette, France*
[15]*ESAC, European Space Astronomy Centre, Villanueva de la Cañada, E-28692 Madrid, Spain*

Accepted 2015 October 23. Received 2015 July 31; in original form 2015 October 24

ABSTRACT

We study the timing and spectral properties of the low-magnetic field, transient magnetar SWIFT J1822.3−1606 as it approached quiescence. We coherently phase-connect the observations over a time-span of ∼500 d since the discovery of SWIFT J1822.3−1606 following the *Swift*-Burst Alert Telescope (BAT) trigger on 2011 July 14, and carried out a detailed pulse phase spectroscopy along the outburst decay. We follow the spectral evolution of different pulse phase intervals and find a phase and energy-variable spectral feature, which we interpret as proton cyclotron resonant scattering of soft photon from currents circulating in a strong ($\gtrsim 10^{14}$ G) small-scale component of the magnetic field near the neutron star surface, superimposed to the much weaker ($\sim 3 \times 10^{13}$ G) magnetic field. We discuss also the implications of the pulse-resolved spectral analysis for the emission regions on the surface of the cooling magnetar.

Key words: stars: individual: SWIFT J1822.3−16066 – stars: magnetar – stars: neutron – X-rays: bursts.

1 INTRODUCTION

Magnetars are isolated neutron stars (NSs) believed to possess very strong magnetic fields ($\sim 10^{14}$–10^{15} G; Duncan & Thompson 1992; Thompson & Duncan 1995) which power their bright X-ray emission, as well as their occasional outbursts and flares. The magnetar class is historically composed of two classes of sources, the Anomalous X-ray Pulsars (AXPs) and Soft γ-ray Repeaters (SGRs), which share a wide range of characteristics, mainly (see Mereghetti 2008 for a review):

(i) spin periods in the 2–12 s range;
(ii) large positive period derivatives (10^{-13}–10^{-10} s s^{-1});
(iii) X-ray luminosities in the range 10^{33}–10^{35} erg s^{-1};

⋆ E-mail: guillermo.rodriguez@oa-roma.inaf.it (GARC); grodriguezcas@gmail.com

(iv) sporadic bursting activity on time-scales from ms to minutes.

While a decade ago their persistent X-ray emission (outside their bursting periods) was believed to be steady. In 2004, Ibrahim et al. (2004) discovered the first transient magnetar, XTE J1810−197. The source was observed at a peak persistent luminosity ∼100 higher that the quiescent value ($\sim 10^{33}$ erg s^{-1}; Gotthelf et al. 2004). Other magnetars have since been discovered which undergo transient outbursts lasting months to years until the quiescence is recovered. Therefore many unidentified faint X-ray sources might host quiescent magnetars that can be identified as they become active. Thanks to the observing capabilities of present space missions such as *Swift*, *INTEGRAL* and *Fermi*, several new magnetars have been discovered through the detection of short bursts events (10–100 ms duration) and/or long-term (months–years) outbursts (see Rea & Esposito 2011 for a review).

The magnetic field strength of magnetars is usually estimated by assuming that, like ordinary pulsars, they spin-down mainly through magnetic dipole losses. The intensity of the dipole magnetic field at the star equator is estimated as $B_{\rm dip} \sim 3.2 \times 10^{19}(P\dot{P})^{1/2}$ G, where P is the spin period in seconds, $\dot{P}$ its first time derivative and an NS with radius $R \sim 10^6$cm and moment of inertia 10^{45} g cm^2 is assumed.

Until some years ago all such measurements led to dipolar field strengths of $\sim 10^{14}$–10^{15} G. However, the monitoring of the outburst of SGR 0418+5729 demonstrated the existence of sources showing typical magnetar-like outbursts and short bursts, but with dipole fields in line with ordinary pulsars (i.e. $\sim 6 \times 10^{12}$ G; Rea et al. 2013). Simulations of magnetic field evolution in NSs with different initial field strength and configuration have shown that, a relatively old magnetar such as SGR 0418+5729 despite its low surface dipolar field, might still harbour a sufficiently intense internal/crustal toroidal field to give rise to outbursts and short X-ray bursts (Turolla et al. 2011).

Two more low-field magnetars were recently discovered thanks to their outburst activity, 3XMM J185246.6+003317 (Rea et al. 2014; Zhou et al. 2014) and SWIFT J1822.3−1606 (Rea et al. 2012; Scholz et al. 2012). The latter source was studied through the long-term monitoring that we present in this work.

1.1 SWIFT J1822.3−1606

The magnetar SWIFT J1822.3−1606 (Swift J1822, hereafter) was discovered through the detection of a series of bursts by the *Swift* Burst Alert Telescope (BAT) and *Fermi* Gamma-ray Burst Monitor (GBM; Cummings et al. 2011) in 2011 July. Soon afterwards Pagani, Beardmore & Kennea (2011) found the position of the new source at RA (J2000): $18^{\rm h}22^{\rm m}18\overset{\rm s}{.}00$ Dec. (J2000): -16d $04'$ $26\overset{''}{.}8$, with 1.8 arcsec radius of uncertainty (90 per cent confidence). Subsequently, the source was followed by virtually all the current generation of X-ray satellites. The results of the first 9 months of X-ray monitoring of this new magnetar were presented and discussed by Rea et al. (2012; hereafter R12), Scholz et al. (2012) and Scholz, Kaspi & Cumming (2014). In this work, we perform an unprecedent coherent, pulse phase resolved spectroscopy (PPS) analysis spanning more than 400 d of outburst decay (see Fig. 1).

2 OBSERVATIONS AND DATA PROCESSING

For the study of the outburst decay, we used data from one *XMM–Newton*, four *Chandra* and 10 *Swift* observations in addition to the data used in R12. We also used the *Chandra* ACIS-S pointings carried out at the beginning of the outburst in order to perform a detailed time-resolved PPS study. A log of the data collected during 2012 is given in Table 1.

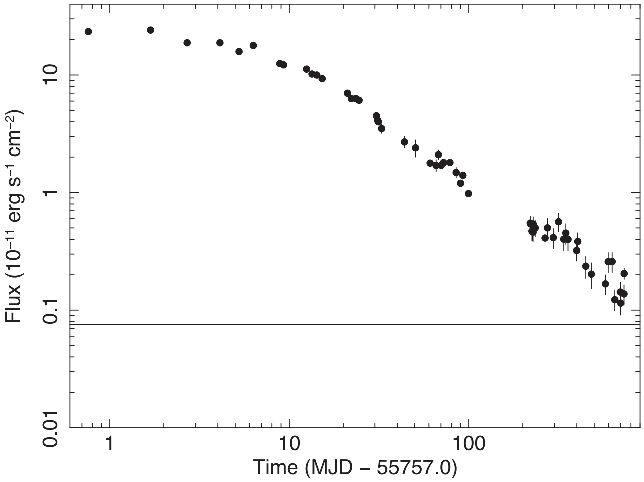

Figure 1. *Swift*-RXT flux decay of Swift J1822.3−1606 in the 1–10 keV energy range. The solid line represents the quiescence flux level.

The data reduction was performed by means of the standard procedures outlined in R12: it consists of initial raw data calibration, filtering from soft-proton flares, correcting the arrival times to the barycenter of the Solar system, source and background extraction, pileup checks, spectral data rebinning and grouping (see Section 2.2.2 for datails). These steps were performed by using the official Science Analysis System (SAS) package (version 11) for the *XMM–Newton* data, and the Chandra Interactive Analysis of Observations (CIAO) system (version 4.4) for the *Chandra* data. The *Swift* data were processed and filtered with standard procedures and quality cuts[1] using FTOOLS tasks in the HEASOFT software package (v. 6.12) and the calibration files from the latest CALDB release.

For the spectral analysis, we used XSPEC (version 12.7.1), for the timing analysis, XRONOS (version 5.22) and pipelines developed in-house for the phase fitting procedures.

2.1 Timing

We begun by extending the validity of the phase-coherent timing solution reported by R12 by adding the new data sets listed in Table 1. In fact, the accuracy and time span between the latest R12 observation and the first of the additional ones listed in Table 1 (∼21 d) is such that we do not miss any cycle in the phase-fitting procedure.

In order to fit the additional data, we added a second period derivative to the timing solution (see Fig. 2, lower panel). The introduction of the higher order period derivative results in a significant improvement of the fit; an F-test gave a probability of $>10\sigma$ that the inclusion of a cubic component is required for our data set (see Fig. 2).

The best timing solution for our data set is $P = 8.437\,720\,019(7)$ s, $\dot{P} = 1.34(1) \times 10^{-13}$s s^{-1} and $\ddot{P} = -5.1(2) \times 10^{-21}$s s^{-2} ($1\sigma$ c.l., three parameters of interest for epoch 55757.0 MJD; see also Table 2). Based on the best fitting P and $\dot{P}$, the inferred surface dipolar magnetic field is $B \sim 3.4(1) \times 10^{13}$ G at the equator. This value lies in between previous results of Scholz et al.

---

[1] See http://swift.gsfc.nasa.gov/docs/swift/analysis/ for more details.

Table 1. Observations used in the timing analysis. In bold are denoted the observations added to those used in R12.

Instrument	Obs.ID	Date^a (MJD TBD)	Exposure (ks)
Swift	00032033001 (PC)	55757.75058	1.6
RXTE	96048-02-01-00	55758.48165	6.5
Swift	00032033002 (WT)	55758.68430	2.0
Swift	00032033003 (WT)	55759.69082	2.0
RXTE	96048-02-01-05	55760.80853	1.7
Swift	00032033005 (WT)	55761.54065	0.5
RXTE	96048-02-01-01	55761.55969	5.0
Swift	00032033006 (WT)	55762.24089	1.8
RXTE	96048-02-01-02	55762.47384	4.9
Swift	00032033007 (WT)	55763.30400	1.6
RXTE	96048-02-02-00	55764.61846	6.1
RXTE	96048-02-02-01	55765.46687	6.8
Swift	00032033008 (WT)	55765.85252	2.2
Swift	00032033009 (WT)	55766.28340	1.7
RXTE	96048-02-02-02	55767.59064	3.0
RXTE	96048-02-02-03	55769.35052	3.4
Swift	00032033010 (WT)	55769.49531	2.1
Swift	00032033011 (WT)	55770.39936	2.1
Chandra	13511	55770.83049	11.7
Swift	00032033012 (WT)	55771.23302	2.1
RXTE	96048-02-03-00	55771.34185	6.8
Swift	00032033013 (WT)	55772.40044	2.1
RXTE	96048-02-03-01	55774.34999	6.9
Chandra	12613	55777.22193	15.0
RXTE	96048-02-03-02	55777.85040	1.9
Swift	00032051001 (WT)	55778.10744	1.7
Swift	00032051002 (WT)	55779.18571	1.7
RXTE	96048-02-04-00	55780.85040	6.7
Swift	00032051003 (WT)	55780.49505	2.3
Swift	00032051004 (WT)	55781.49878	2.3
RXTE	96048-02-04-01	55782.57749	6.2
RXTE	96048-02-04-02	55784.97179	6.2
Swift	00032051005 (WT)	55786.42055	2.2
Swift	00032051006 (WT)	55787.58688	2.2
RXTE	96048-02-05-00	55788.05419	6.0
Swift	00032051007 (WT)	55788.25617	2.3
Swift	00032051008 (WT)	55789.66173	1.7
RXTE	96048-02-05-01	55789.95880	6.0
Swift	00032051009 (WT)	55790.36270	2.2
RXTE	96048-02-06-00	55794.45899	6.5
RXTE	96048-02-07-00	55799.61550	6.9
Swift	00032033015 (WT)	55800.86278	2.9
Swift	00032033016 (WT)	55807.48660	2.4
RXTE	96048-02-08-00	55810.37979	6.0
Suzaku/XIS	906002010	55817.92550	33.5
RXTE	96048-02-10-00	55820.23970	6.7
Chandra	12614	55822.79364	10.1
Swift	00032033017 (WT)	55822.82836	4.9
Swift	00032033018 (WT)	55824.71484	1.5
RXTE	96048-02-10-01	55826.18540	5.6
XMM–Newton	0672281801	55827.25350	10.6
Swift	00032033019 (WT)	55829.45421	2.3
Swift	00032033020 (WT)	55835.54036	2.6
RXTE	96048-02-11-00	55835.90370	7.0
Swift	00032033021 (WT)	55842.06040	4.2
RXTE	96048-02-12-00	55842.23269	5.8
XMM–Newton	0672282701	55847.06380	25.8
Swift	00032033022 (WT)	55849.61916	3.4
RXTE	96048-02-13-00	55849.6597976	5.6
Swift	00032033024 (WT)	55862.59155	10.2
RXTE	96048-02-14-00	55863.11100	5.6
Chandra	12615	55867.17461	16.3
Swift	00032033025 (PC)	55977.16600	6.3
Swift	00032033026 (WT)	55978.53399	10.2
Swift	00032033027 (PC)	55981.99499	11.0
Swift	00032033028 (WT)	55982.96299	7.0
Swift	00032033029 (WT)	55985.17799	7.0
Swift	00032033030 (WT)	55985.55000	7.0
Swift	00032033031 (WT)	55991.09231	6.7
XMM–Newton	0672282901	56022.95692	26.9
Swift	00032033032 (WT)	56031.141159	4.3
Chandra	14330	56037.08846	20.1
Swift	00032033033	56052.66948	5.2
Swift	00032033034	56073.25354	4.9
Swift	00032033035	56095.56083	5.6
Swift	00032033036	56104.55201	6.2
Swift	00032033037	56114.31112	6.8
Swift	00032033038	56136.32359	9.0
Swift	00032033039	56156.20958	4.9
Swift	00032033040	56161.69589	5.0
XMM–Newton	0672283001	56178.85111	21.7
Swift	00032033042	56206.00752	5.0
Swift	00032033043	56238.70919	4.9

Note. ^{a}Mid-point of the observations.

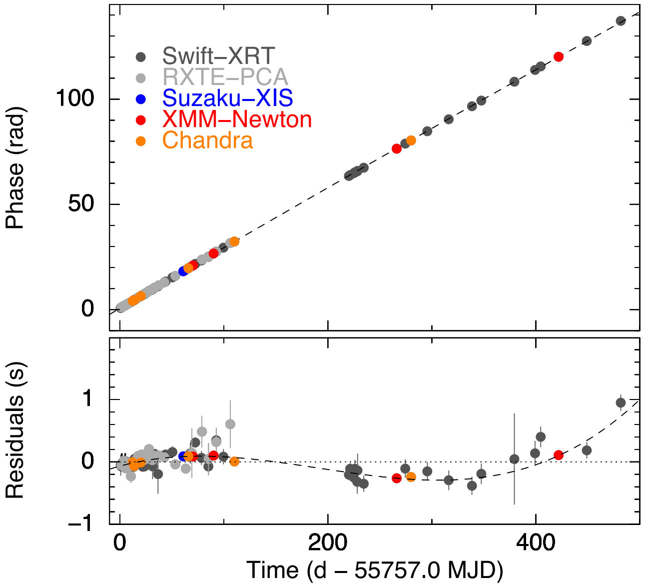

Figure 2. Pulse phase evolution over time. In the lower panel are shown the time residuals after correcting the linear and quadratic components (correction to the P and $\dot{P}$ values). The dashed line in the residual panel marks the detected $\ddot{P}$ component. The epoch of reference is 55757.0 Modified Julian Date (MJD). See the text for details on the ephemerides.

(2012): $B \sim 5 \times 10^{13}$ G, and R12: $B \sim 2.7 \times 10^{13}$ G, and is higher than the estimate of Scholz et al. (2014): $B \sim 1.4 \times 10^{13}$ G. Yet, it is lower than the $\mathrm{B_{QED}}$ critical value ($B \sim 4.4 \times 10^{13}$ G): SWIFT J1822.3−1606 is thus the magnetar with the second lowest magnetic field. This timing solution also implies a spin-down power $L_{\rm rot} = 4\pi^2 I \dot{P}/P^3 \sim 9 \times 10^{30}$ erg s^{-1}, assuming uniform-density NS with moment of inertia $I = 10^{45}$ g cm^2. The inclusion of a third period derivative, or other components, such as a post-glitch recovery, does not significantly improve the fit. However, the timing

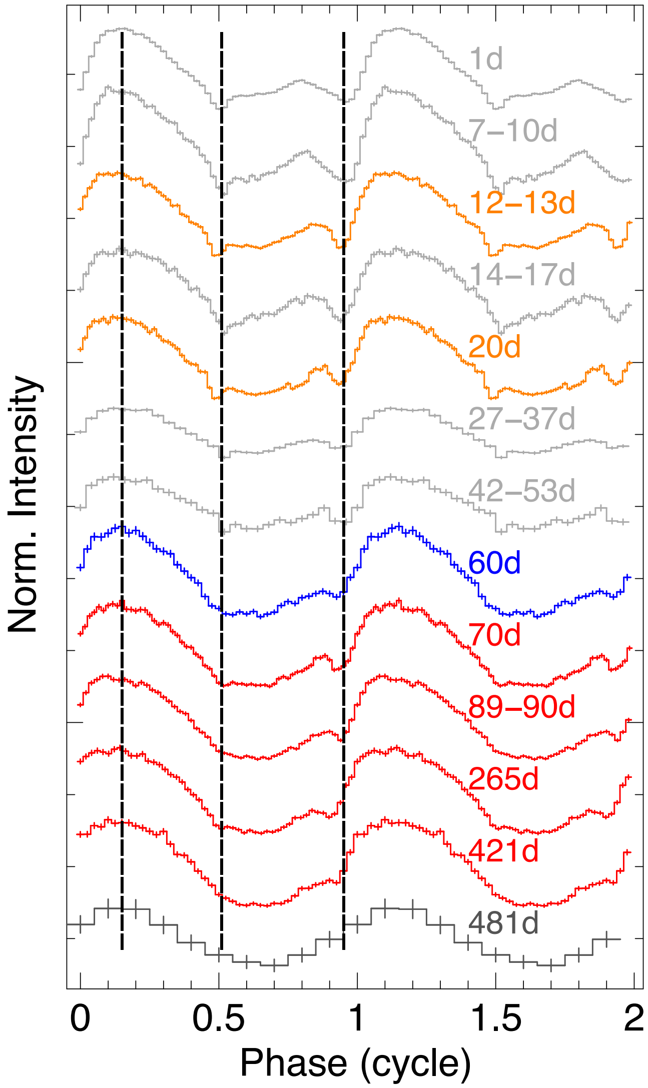

Figure 3. Selected pulse shapes plotted as a function of time for different epochs of the 2011–2012 outburst of SWIFT J1822.3−1606. The 1–10 keV light curves (2–10 keV for *RXTE*) have been folded to the $P-\dot{P}-\ddot{P}$ phase-coherent solution reported in Table 2. Different colours mark data from different missions similarly to the colour code used in Figure 2.

Table 2. Timing parameters for SWIFT J1822.3−1606.

Reference Epoch (MJD)	55757.0
Validity period (MJD)	55757– 56239
P (s)	8.437 720 019(7)
$\dot{P}$ (s s^{-1})	1.34(1) × 10^{-13}
$\ddot{P}$ (s s^{-2})	−5.1(2) × 10^{-21}
ν (Hz)	0.1185154281(1)
$\dot{\nu}$(s^{-2})	−1.88(2) × 10^{-15}
$\ddot{\nu}$(Hz s^{-2})	7.1(2) × 10^{-23}
χ^2/dof	168/81
RMS residuals (ms)	360
B (Gauss)	∼3.4 × 10^{13}
$L_{\rm rot}$ (erg s^{-1})	∼8.9 × 10^{30}
$\tau_{\rm c}$ (Myr)	∼1.0

solution by Scholz et al. (2014) over a longer – with respect to this work – time span of ∼2.3 yr did indeed improve with the inclusion of an exponential glitch recovery for the first ∼60 d, and a separate $P-\dot{P}$ timing solution for the rest of the data set, see Scholz et al. (2014) for details on their solution. For the purpose of this work, a single coherent timing solution for the entire data set is desirable and we use our timing solution to perform the pulse phase-resolved analysis. We note that the timing solutions with parameters closer to ours are those reported by R12 and the 2nd solution of Scholz et al. (2012), which were obtained over a time-span of ∼1 yr.

2.2 Spectral analysis

2.2.1 *Phase-average analysis*

Phase-averaged spectral analysis were performed by R12, Scholz et al. (2012) Scholz et al. (2014). In all cases, a model composed by a photoelectrically absorbed blackbody (BB) plus a power-law (PL) was used to fit the spectra; in R12 a two-BB was used as well. In both Scholz et al. (2012) and Scholz et al. (2014), acceptable fits were obtained in the 1–10 keV band. In R12 over the 0.6–10 keV energy band (for both models). Restricting the *XMM–Newton* data to those energy intervals, we were able to reproduce their results for all the common *XMM–Newton* spectra. However, the situation changes when we considered a larger energy range, 0.3–10 keV.

Indeed, the two-BB model failed to fit the high-energy part (>6 keV) of the spectra (see e.g. Fig. 4, upper panel, where a $\chi^2_{\rm red} = 2.31$ for 674 degrees of freedom, dof was obtained). Following the same rationale as in the case of CXOU J164710.2−455216 (Rodríguez Castillo et al. 2014), we added an additional ('cold') BB with fixed temperature to the two-BB model. Thus, adding one additional parameter to the fit, namely, the cold BB radius. This additional component is meant to account for a colder surface region, which might correspond to either the rest of the NS surface, or a portion of it. The $kT_{\rm BB} \sim 150$ eV value is based on spectral analysis of the quiescent emission of SWIFT J1822.3−1606, previously performed in R12 and Scholz et al. (2012). Note that estimates for other magnetars (i.e. XTE J1810−197 and CXOU J164710.2−455216, see Albano et al. 2010) yield similar values.

The addition of the colder BB yields an improved $\chi^2_{\rm red}$ of 1.08 (670 dof, see Fig. 4 and Table 3). We studied the significance of such component by calibrating the F-statistics using simulations of the null model (the double-BB model) as suggested by Protassov et al. (2002). In accordance with this approach, the distribution of the null F-statistic was produced by fitting each simulated spectrum with both the null and the triple-BB model and extracting the relative F-statistic. Running 5 × 10^5 Monte Carlo simulations, we obtained that the chance occurrence probability of such an improvement is lower than 2 × 10^{-6}.

Besides significantly improving the fits, the 1(T-fixed)+2(free) BB (1+2BB, for short) model provides consistent results. First, the radius, which is the only free parameter of the additional, temperature-fixed BB, varies from $4.0\,d_{1.6}$ km to $7.3\,d_{1.6}$ km, where $d_{1.6}$ is the distance to the magnetar in units of 1.6 kpc, the value proposed by Scholz et al. (2012, see below). Another hint at the validity of the model is the fact that the measured radius of the cold component is consistent with the BB radius observed in quiescence, before the outburst, at the same temperature (R12; Scholz et al. 2012). Note as well that the measured radius, both in our analysis as well as in the cited papers, is significantly less than the expected ∼10 km for an NS, suggesting that it may not correspond to the whole surface.

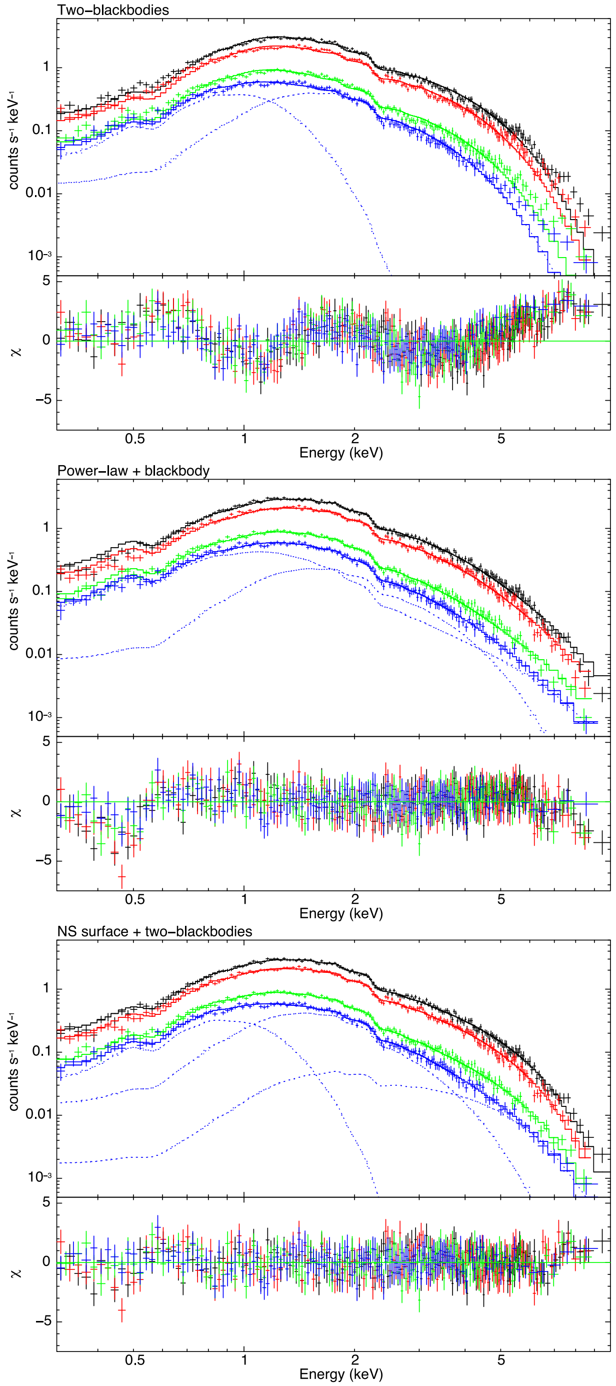

Figure 4. SWIFT J1822.3−1606 *XMM–Newton* spectra. Best fits using 2-blackbodies (upper panel), BB plus PL (middle panel), and 2+1-blackbodies (lower panel). $\chi^2_{\rm red}$ = 2.31, 1.44 and 1.08, respectively. The fits components of the last observations (blue dotted lines) are shown for comparison. Note that by the last observation the source has significantly softened and the hot BB component is not dominant. See the text for details.

On the other hand, the PL+BB model, while fitting well the data in the 0.6–10 keV range (R12), shows significant residuals at lower energies <0.6 keV (see Fig. 4, middle panel). In the 0.3–10 keV range, the PL+BB model yields a poor $\chi^2_{\rm red}$ /dof = 1.44 /674. In the case of the PL+BB model, adding the same temperature-fixed BB, as it was done for the 2BB model, only marginally improves the fit ($\chi^2_{\rm red}$ /dof = 1.22 /670).

Using the best 1(T-fixed)+2(free), BB model and the whole set of phase-average spectra, we obtained a best-fitting column density value of $N_{\rm H} = 4.7(1) \times 10^{21}$ cm^{-2}, which is very close to the values found in previous works, R12 $N_{\rm H}$ = 5.0(1) × 10^{21} cm^{-2} ; and Scholz et al. (2012) $N_{\rm H} = 4.5(1) \times 10^{21}$ cm^{-2}. Moreover, this value is consistent with the $N_{\rm H}$ = 4(1) × 10^{21} cm^{-2} of the Galactic H II region M17 (Townsley et al. 2003), located about 20 arcmin from Swift J1822 and at 1.6 ± 0.3 kpc from us (Nielbock et al. 2001), as noted by Scholz et al. (2012). We kept $N_{\rm H}$ fixed at 4.7 × 10^{21} cm^{-2} for the rest of the analysis, and adopted a tentative distance of 1.6 kpc in BB radii calculations.

For this analysis, the solar abundances by Anders & Grevesse (1989) were used to account for the photoelectric absorption, the same used in all previous analysis (R12; Scholz et al. 2012). In addition, we used the same photoelectric cross-sections by Balucinska-Church & McCammon (1992) used in the cited works. We also tried other solar abundances (Feldman 1992; Wilms, Allen & McCray 2000; Lodders 2003; Asplund et al. 2009) and in all cases the 1+2BB model showed a similar statistical predominance in comparison to the PL+BB and the 2BB models as described above.

2.2.2 *Coherent phase-resolved analysis*

In this section, we describe a pulse phase resolved analysis as a function of the decaying flux by using one *Chandra* plus the four *XMM–Newton* pointings covering the outburst decay from day 12 up to day 421. To do so, we use our updated phase-coherent timing solution to fold and extract the spectra.

In order to define the phase interval selection, we inspected spectral changes across the pulse profile in single observations (see e.g. Fig. 5). A pulse profile comparison as a function of time is shown in Fig. 6. In both figures similar features are seen in the same phase regions, near phase 0.5 and 0.93. Based on this and in order to make sure that each phase interval contains enough counts, we adopted the phase intervals marked as P1, P2, P3 and P4 in Fig. 6, which correspond to phases 0.05–0.4, 0.4–0.55, 0.55–0.9 and 0.9–1.05, respectively.

For the spectral fitting (with XSPEC version 12.7.1), the data were grouped so as to have at least 30 counts per energy bin, while the instrument energy resolution were oversampled by a factor of 3. The standard routines of XMM-SAS and CIAO were used to produce the ancillary response files and redistribution matrix files.

For the phase-resolved spectroscopy, we used the 2(free)+1(T-fixed) BB model described above (Section 2.2.1). We also assume that the geometric configuration of the emission zones does not vary dramatically during the outburst decay, so we follow each evolving component during the outburst decay. The observed pulse profile relative stability over time (see e.g. Fig. 6) indicates that these assumptions are reasonable. In the context of our spectral analysis, we interpret the flux evolution (Fig. 1) as changes in the radii and temperature of the two free blackbodies. Since no geometric information about the specific configuration of the emission zones is available, the two blackbodies were left free to vary from phase to phase, in the case that more than one hot region is present. We favour a two-hotspot (emission zones) model (see Section 3), since a single hotspot configuration does not reproduce the observed pulse profiles. The results are presented in Table 4 and graphically in Figs 7–9, where phase intervals P1 and P3 are shown in the upper panels and P2 and P4 in the lower panels. The phase intervals have been divided in this way for visualization purposes and because of similarities found in some intervals, in particular, between P2 and

Table 3. Parameters of 1+2BB fit of *Chandra* (MJD 15777) and *XMM–Newton* spectra (See text for details on the model). The distance used to calculate the R_{BB} was 1.6 kpc, as proposed by Scholz et al. (2012). Error are 1-σ.

SWIFT J1822.3−1606 1+2-BB phase-average spectral fit					
Obs. MJD	T_h (keV)	R^h_{BB} (Km)	T_w (keV)	R^w_{BB} (Km)	R^c_{BB} (Km)
15777	$1.07^{+0.04}_{-0.03}$	0.29 ± 0.02	0.52 ± 0.01	1.26 ± 0.04	11.6 ± 0.2
15827	$0.87^{+0.04}_{-0.03}$	0.23 ± 0.02	0.41 ± 0.02	$0.96^{+0.05}_{-0.04}$	7.0 ± 0.3
15846	0.83 ± 0.03	0.22 ± 0.01	0.41 ± 0.02	0.82 ± 0.04	6.3 ± 0.3
16023	0.87 ± 0.03	$0.10^{+0.02}_{-0.01}$	0.42 ± 0.02	$0.54^{+0.02}_{-0.03}$	4.52 ± 0.2
16178	$0.98^{+0.10}_{-0.08}$	$0.05^{+0.02}_{-0.01}$	0.48 ± 0.02	$0.36^{+0.02}_{-0.03}$	4.2 ± 0.2

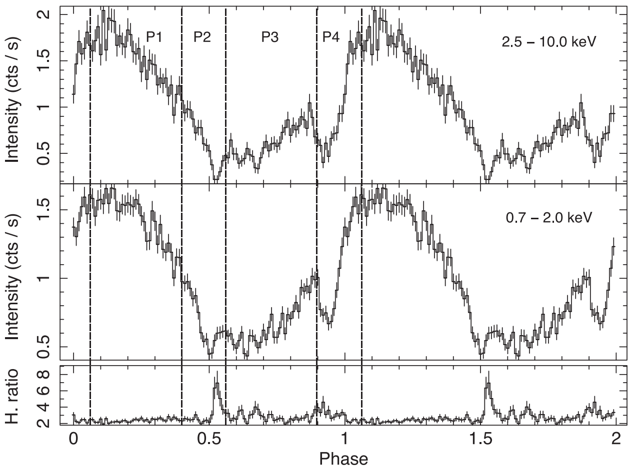

Figure 5. Pulse profile of SWIFT J1822.3−1606 in the 2.5–10 keV interval (upper panel); 0.7–2 keV interval (middle panel) and hardness ratio for those intervals (lower panel). Obs id: 0672281801.

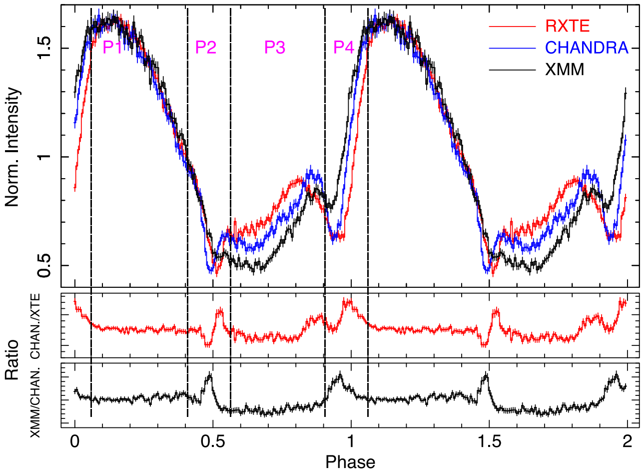

Figure 6. Upper panel: 0.3–10 keV normalized pulse profiles for the highest statistics light curves which are also a function of increasing time and decreasing flux from the outburst onset: *RXTE*, *Chandra* and *XMM–Newton* in the order of decreasing flux (see also Fig. 3). Lower panels: ratios of the profiles used to identify the phase interval with larger pulse profile variations.

P4, which show quite similar values and evolution throughout the outburst decay (see Section 3).

In order to maintain coherence with previous works and with our phase-averaged analysis, we used the Anders & Grevesse (1989) solar abundances and corrected the photoelectric absorption with Balucinska-Church & McCammon (1992) photoelectric cross-sections in the PPS as well. We note that since different solar abundances affect only the lower energies, only the radius of the fixed, cold BB, is affected (reduced it by a factor of $\lesssim 2$). The warm and hot BB, (see Table 4) remain unaffected within the 1σ confidence interval, when the solar abundances are varied (see also Section 2.2.1).

2.2.3 *Phase-variable spectral features*

To better explore the complex variability with phase of the X-ray spectrum of SWIFT J1822.3−1606, we created phase-energy images from the X-ray observations with the best counting statistics and enough spectral/time resolution, by binning the source counts into small phase and energy intervals (see Figs 10 and 11). This kind of analysis has proven useful to identify possible narrow spectral features that strongly vary with phase, like the absorption-like feature discovered in SGR 0418+5729 (Tiengo et al. 2013; hereafter T13).

A dark straight line, slightly inclined to the right, is visible at phase ~0.5 in the *RXTE*, *Chandra* and *XMM–Newton* images (Figs 10 and 11). In addition, the uppermost panel of Fig. 11 obtained with *RXTE* data of energies >4 keV, displays a dark 'V'at phase ~0.9–1.1, similar to the one detected in the phase-energy images of SGR 0418+5729 (T13). The same feature cannot be clearly detected in the *Chandra* and *XMM–Newton* data likely due to poorer statistics at high energies.

These dark tracks are rather narrow and almost vertical, suggesting the presence of an absorption-like line in the spectrum, whose energy rapidly varies with phase. As in T13, 50 phase-resolved spectra for each of the three data sets were extracted and analysed with simple spectral models. Due to the relatively small number of counts in each phase interval, all the *XMM–Newton* spectra were consistent with the model of the phase-averaged spectrum, simply rescaled by a flux normalization factor. On the other hand, the *RXTE* phase-resolved spectra displayed significant differences, which motivated a detailed analysis.

A template spectral model was derived by fitting the *RXTE*/PCA spectrum extracted from the 0.6–0.8 phase interval, where the phase-energy image shows no narrow-band spectral variability. For consistency with the previous analysis, we adopted a three BB model with photoelectric absorption fixed at $N_{\rm H} = 4.7 \times 10^{21}$ cm^{-2} and one of the three BB components with $kT = 150$ eV and $R_{\rm BB} = 10$ km (assuming a distance of 1.6 kpc).[2] A good fit is obtained only by adding a Gaussian emission line with $E = 6.47 \pm 0.06$ keV, $\sigma = 0.3 \pm 0.1$ keV and flux of $(4 \pm 1) \times 10^{-4}$ photons cm^{-2} s^{-1}, possibly due to an incorrect reconstruction of the Galactic Ridge component in the PCA background model. In this case, the temperatures of

---

[2] Since the PCA spectra are analysed only for $E > 2.5$ keV, this soft BB component gives a negligible contribution to the spectral fit.

Table 4. 1+2BB fit spectral parameters of the phase resolved spectroscopy. The distance used to calculate the R_{BB} was 1.6 kpc, as proposed by Scholz et al. (2012). Reported error are 1σ.

SWIFT J1822.3−1606: 1+2-BB spectral fit						
Pulse phase interval[a]	Obs. MJD	T_h (keV)	R^h_{BB} (km)	T_w (keV)	R^w_{BB} (km)	R^c_{BB} (km)[b]
	15777	$1.24^{+0.08}_{-0.07}$	$0.26^{+0.04}_{-0.03}$	$0.56^{+0.01}_{-0.02}$	1.48 ± 0.04	14.5 ± 0.3
	15827	$0.95^{+0.04}_{-0.03}$	$0.23^{+0.03}_{-0.02}$	0.46 ± 0.02	1.01 ± 0.05	8.9 ± 0.2
P1	15846	0.89 ± 0.03	0.22 ± 0.02	0.43 ± 0.02	$0.94^{+0.06}_{-0.05}$	7.8 ± 0.2
$\chi^2_{\mathrm{red}} = 1.1865$	16023	0.84 ± 0.03	0.14 ± 0.02	0.44 ± 0.02	$0.68^{+0.05}_{-0.04}$	5.1 ± 0.1
	16178	$0.94^{+0.10}_{-0.08}$	$0.07^{+0.03}_{-0.02}$	0.46 ± 0.02	0.44 ± 0.03	4.6 ± 0.1
	15777	$1.05^{+0.10}_{-0.08}$	$0.25^{+0.05}_{-0.07}$	0.48 ± 0.03	$1.19^{+0.12}_{-0.08}$	11.2 ± 0.4
	15827	$0.89^{+0.06}_{-0.05}$	0.19 ± 0.03	0.38 ± 0.04	$1.0^{+0.2}_{-0.1}$	6.9 ± 0.4
P2	15846	$0.82^{+0.05}_{-0.04}$	0.19 ± 0.03	0.39 ± 0.03	$0.79^{+0.14}_{-0.09}$	6.0 ± 0.3
$\chi^2_{\mathrm{red}} = 1.0522$	16023	$1.0^{+0.2}_{-0.1}$	$0.06^{+0.04}_{-0.02}$	$0.47^{+0.03}_{-0.04}$	$0.38^{+0.05}_{-0.04}$	4.5 ± 0.2
	16178	$1.0^{+0.9}_{-0.2}$	$0.02^{+0.13}_{-0.01}$	$0.50^{+0.05}_{-0.07}$	$0.29^{+0.06}_{-0.03}$	4.1 ± 0.2
	15777	$0.89^{+0.04}_{-0.03}$	0.38 ± 0.04	0.43 ± 0.03	$1.27^{+0.12}_{-0.09}$	11.2 ± 0.3
	15827	0.75 ± 0.02	0.28 ± 0.02	0.33 ± 0.03	$1.1^{+0.2}_{-0.1}$	6.0 ± 0.3
P3	15846	$0.76^{+0.03}_{-0.02}$	0.22 ± 0.02	0.36 ± 0.03	$0.75^{+0.12}_{-0.08}$	5.6 ± 0.2
$\chi^2_{\mathrm{red}} = 1.0516$	16023	$0.93^{+0.09}_{-0.07}$	$0.07^{+0.02}_{-0.01}$	0.43 ± 0.03	$0.41^{+0.04}_{-0.03}$	4.5 ± 0.1
	16178	>0.67	$0.002^{+0.029}_{-0.002}$	$0.55^{+0.01}_{-0.03}$	$0.24^{+0.02}_{-0.01}$	4.4 ± 0.1
	15777	$1.00^{+0.09}_{-0.07}$	$0.30^{+0.08}_{-0.06}$	$0.51^{+0.02}_{-0.03}$	$1.38^{+0.08}_{-0.06}$	11.4 ± 0.5
	15827	0.78 ± 0.03	$0.32^{+0.04}_{-0.03}$	0.35 ± 0.03	$1.4^{+0.3}_{-0.2}$	7.0 ± 0.5
P4	15846	$0.80^{+0.09}_{-0.06}$	$0.23^{+0.07}_{-0.06}$	0.44 ± 0.05	$0.76^{+0.13}_{-0.07}$	7.6 ± 0.3
$\chi^2_{\mathrm{red}} = 1.0516$	16023	$0.91^{+0.10}_{-0.07}$	$0.09^{+0.03}_{-0.02}$	0.42 ± 0.03	$0.57^{+0.07}_{-0.05}$	4.8 ± 0.2
	16178	$1.0^{+0.3}_{-0.2}$	$0.04^{+0.05}_{-0.02}$	$0.48^{+0.03}_{-0.04}$	$0.37^{+0.05}_{-0.03}$	4.5 ± 0.2

Notes. [a] See Fig. 6 for reference.

[b] Different solar abundances can reduce this value up to a factor of ∼2. See also Section 2.2.1.

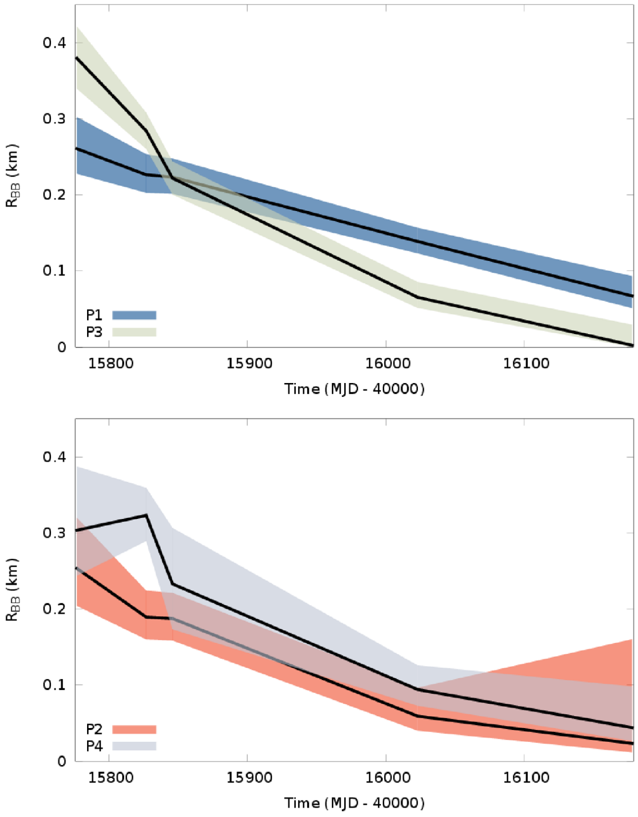

Figure 7. Evolution of the hot blackbodies radii (R_{BB}) used for modelling the pulse phase intervals, see the text for details. The shadows represent the 1σ confidence interval.

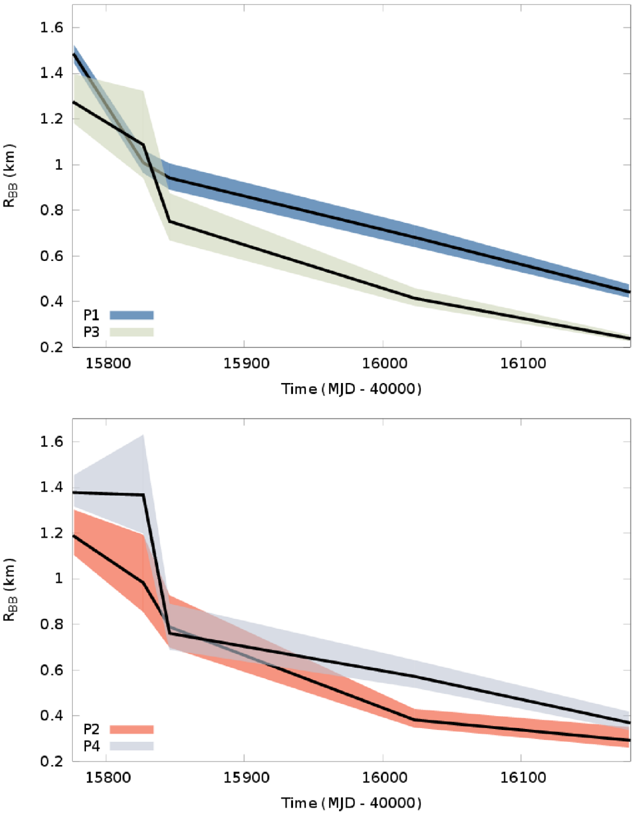

Figure 8. Same as Fig. 7, for the warm blackbodies.

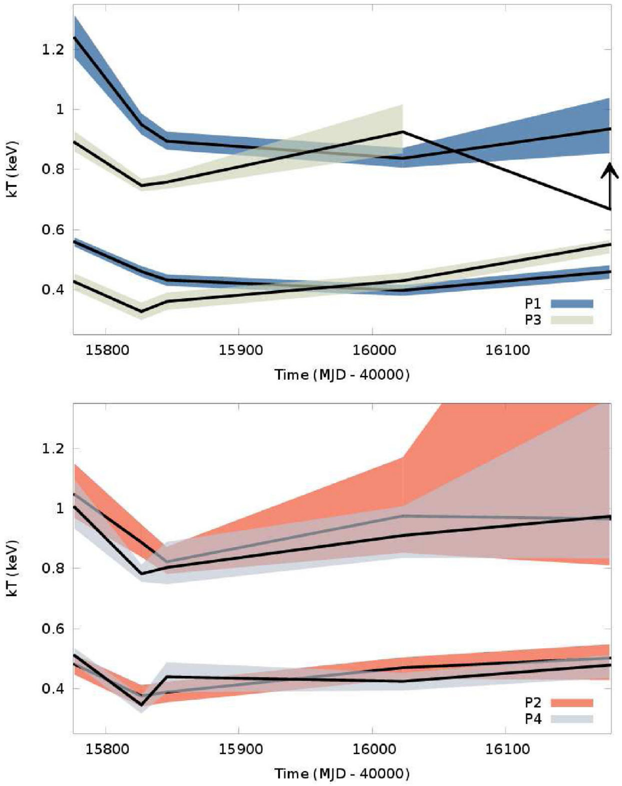

Figure 9. Temperature evolution of the blackbodies used for modelling the pulse phase intervals. Lower values correspond to the warm components, higher values to the hot components. The shadows represent the 1σ confidence interval.

the two variable BB components are: $kT_{\mathrm{h}} = 1.7 \pm 0.1$ keV and $kT_{\mathrm{w}} = 0.73 \pm 0.02$ keV. As can be seen in the lowermost panel of Fig. 12, this template model rescaled by an overall multiplicative factor (except for the Gaussian component, which, consistently with its background interpretation, is kept fixed in all spectra) does not adequately fit the spectra (null hypothesis probability <0.01) in the phase intervals 0.03–0.29, 0.49–0.51, and 0.87–0.99. Acceptable fits were obtained by adding a cyclotron absorption line feature (Makishima et al. 1990) to the model in these phase intervals. The resulting line centroids and widths are shown in Fig. 12.

3 RESULTS AND DISCUSSION

We studied the long-term evolution of the magnetar SWIFT J1822.3−1606, by following the source during its approach to quiescence after the outburst that led to its discovery on 2011 July 14. We performed a timing analysis by phase-connecting observations covering about 500 d of the SWIFT J1822.3−1606 outburst decay. The resulting values of the spin period and period derivative are $P = 8.437\,720\,019(7)$ s and $\dot{P} = 1.34(1) \times 10^{-13}\mathrm{s\ s^{-1}}$, which, if interpreted in terms of magneto-dipolar braking, lead to a value of the dipolar magnetic field of $B \sim 3.4(1) \times 10^{13}$ G at the equator of the star. This confirms that SWIFT J1822.3−1606 is the magnetar with the second lowest dipolar magnetic field detected so far. By performing a timing analysis, we found a significant second time derivative of the period, $\ddot{P}=-5.1(2) \times 10^{-21}\mathrm{s\ s^{-2}}$, which is consistent with the upper limit reported by R12 and with solution 2 of Scholz et al. (2012) and in Scholz et al. (2014) a longer time span is split and fitted with an exponential glitch recovery for the first ∼60 d and an additional P-$\dot{P}$ solution for the rest of their data set, obtaining a somewhat lower estimate of the dipolar magnetic field of $B \sim 1.4 \times 10^{13}$ G.

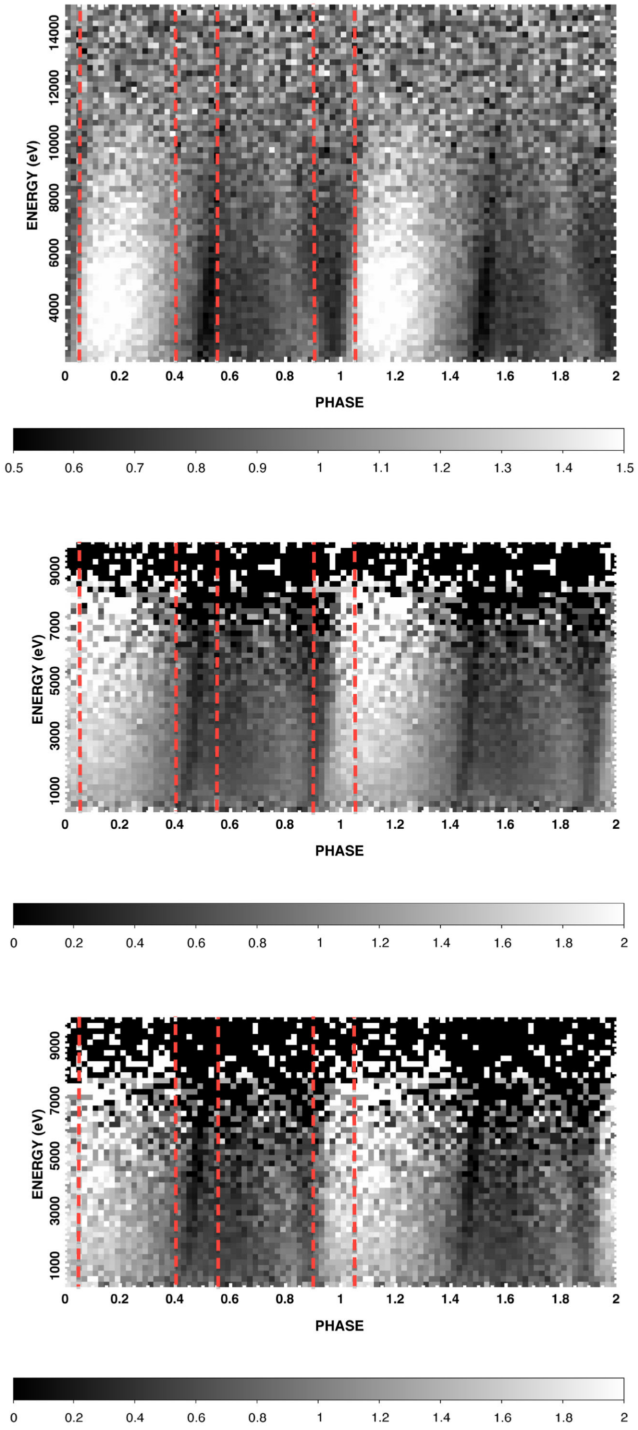

Figure 10. Phase-energy images, divided by the phase-average spectrum, of SWIFT J1822.3−1606 from *RXTE* (PCA observations from 2011 July 16 to 2011 July 20, *top panel*), *Chandra* (ACIS-S observation in CC mode on 2011 July 27, *middle panel*) and *XMM–Newton* (EPIC pn observation on 2011 September 23 *bottom panel*) data. The vertical dashed lines denote the intervals used in the PPS (see Fig. 6).

A closer look at the PPS results shows however that, apart from the above mentioned common characteristics, the spectral evolution

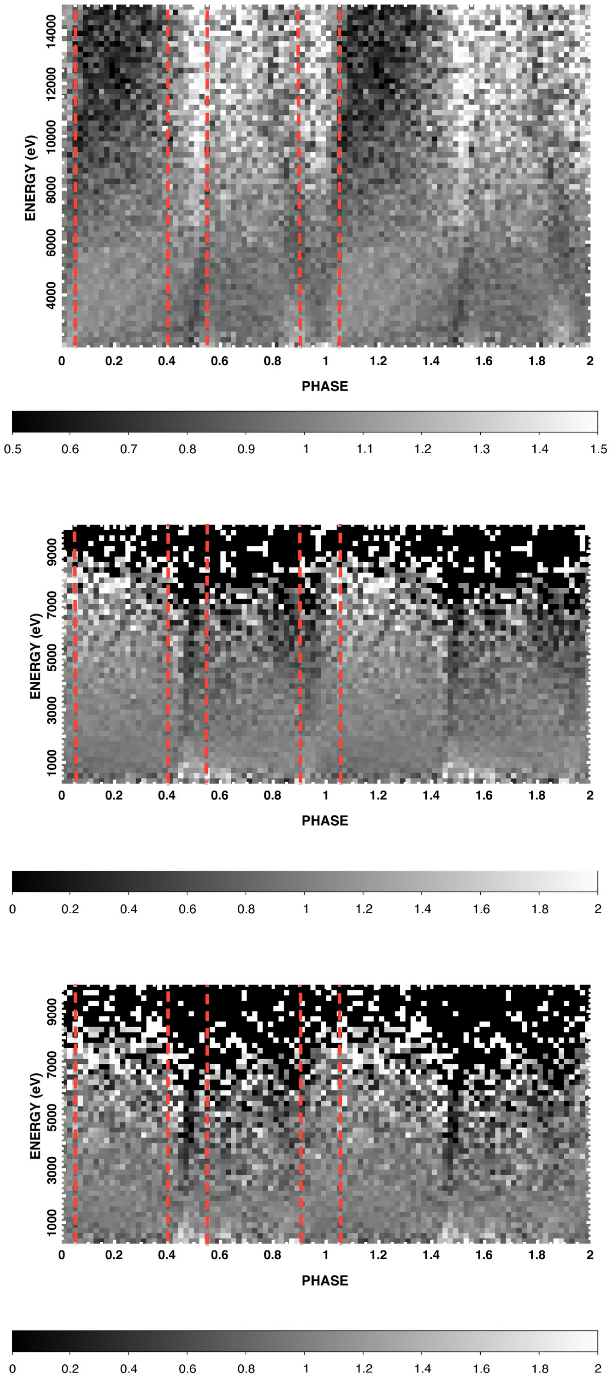

Figure 11. Normalized phase-energy images, divided by the phase-average spectrum and the energy -integrated pulse profile, of SWIFT J1822.3−1606 from *RXTE* (PCA observations from 2011 July 16 to 2011 July 20, *top panel*), *Chandra* (ACIS-S observation in CC mode on 2011 July 27, *middle panel*) and *XMM–Newton* (EPIC pn observation on 2011 September 23 *bottom panel*) data. The vertical dashed lines denote the intervals used in the PPS (see Fig. 6).

of the source at phase intervals P1 and P3 is markedly different from that observed at P2 and P4. The evolution of the spectra at phase intervals P2 and P4 is very similar (see lower panels of Figs 7–9) in terms of both measured values of BB radii and temperatures at each epoch, and in terms of shrinking and cooling rates. Instead, spectra observed at phase intervals P1 and P3 have different initial

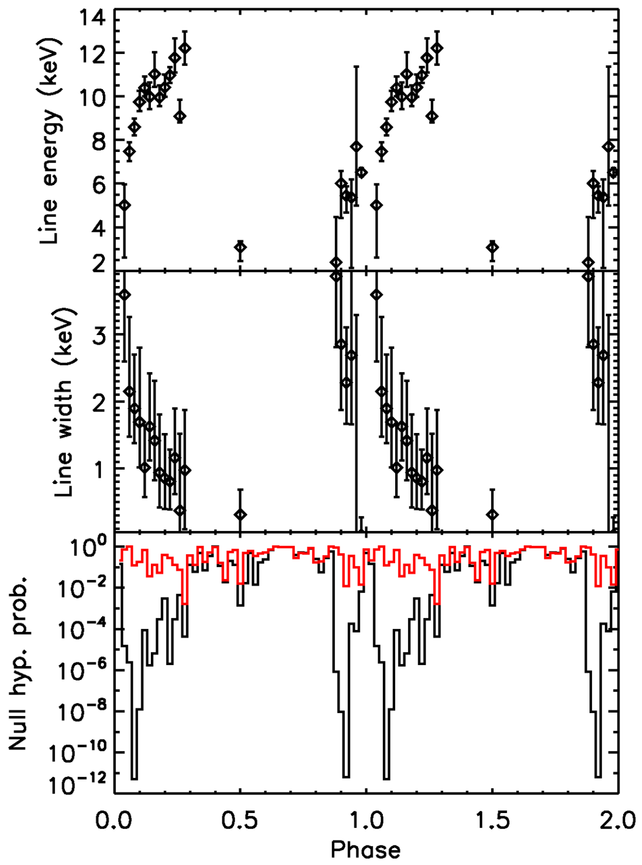

Figure 12. Results of the analysis of 50 phase-resolved spectra of SWIFT J1822.3−1606 during the *RXTE* observations from 2011 July 16 to 20. The energy and width of the line is displayed in the upper panels for the phase intervals that were not adequately fit (null hypothesis probability <0.01) by the model without absorption line. The bottom panel shows the null hypothesis probabilities of the fits of each phase-resolved spectrum with the best-fitting model of the spectrum extracted from the 0.6–0.8 phase interval (see the text for details; *black*) and after the addition of an absorption line (*red*).

values of the BB radii and temperatures and then display different shrinking and cooling rates over the outburst decay (see upper panels of Figs 7–9). This may suggest that, during the phase intervals P1 and P3, we are observing two zones with physically distinct properties, likely the two main surface zones that had been heated during the outburst. Instead, during the phase intervals P2 and P4, we observe a transition, with one of the two heated zones exiting and the second one entering into view. The fact that the temperatures of P2 and P4 are consistently *in between* those of P1 and P3 and that the shape of the observed pulse profile is hardly compatible with a single hotspot, reinforces this two-zones interpretation. We therefore suggest the possibility that the emission is coming from (at least) two zones of the NS surface with different physical properties, the evolution of which may be due to different mechanisms. The BB radius $R_{\rm BB}$ obtained from our spectral fits may not provide a direct measure of the size L of the emitting region on the star surface. In fact, knowledge of the viewing geometry of the source (i.e. magnetic and spin axis inclinations with respect to the line of sight) and of the location of the emitting regions on the star surface would be required to relate L to $R_{\rm BB}$. An evaluation of the source geometry will not be attempted here (although this might be possible; see e.g. Albano et al. 2010). We just note that, since these angles are not

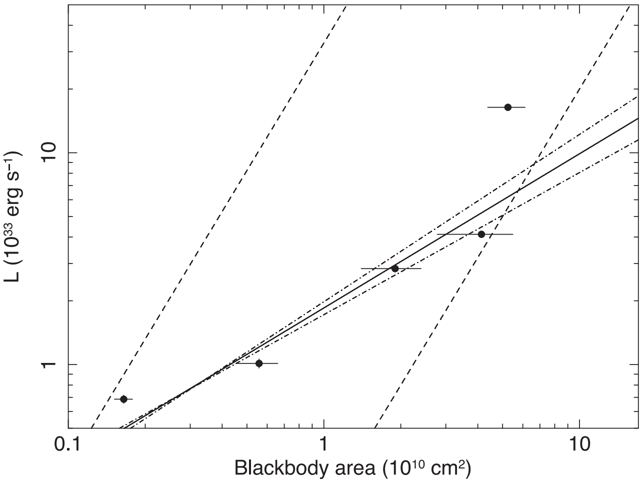

Figure 13. Luminosity versus BB emitting area of the P3 warm component (See Fig. 6 for reference). The dashed lines represent $L \propto A^2$, simple UM models, see Beloborodov (2009). The solid line is a PL fit to the data, which yields $L \propto A^{0.7}$. The 3σ uncertainty of the fit parameters is represented by dot–dashed lines.

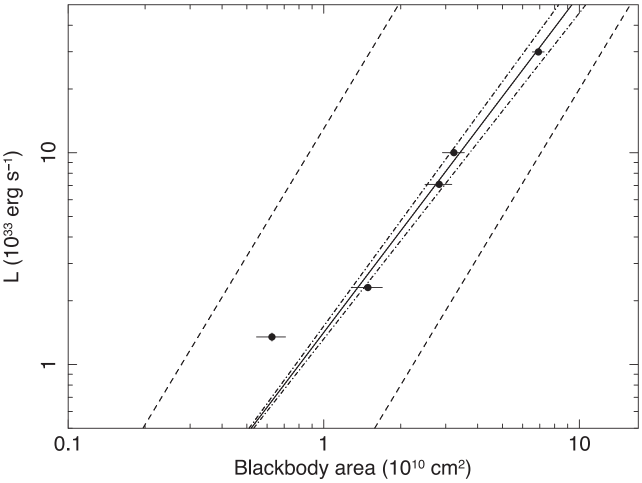

Figure 14. Same as Fig. 13, for P1. The solid line is a PL fit to the data, which yields $L \propto A^{1.6}$. The 3σ uncertainty of the fit parameters (corresponding to $L \propto A^{1.5}$ and $L \propto A^{1.7}$) is represented by dot–dashed lines.

expected to change during the outburst decay, the time evolution of $R_{\rm BB}$ mirrors that of L, that is to say that the rate of change of the two quantities is the same.

The evolution observed during the decay phase of an outburst is usually interpreted in terms of either the cooling that follows deep crustal heating (Perna & Pons 2011) or untwisting of the star magnetosphere (Beloborodov 2009). The overall behaviour of SWIFT J1822.3−1606 i.e. the shrinking of the heated zones at an almost constant temperature, is expected in the framework of both models. For instance, in the untwisting magnetosphere (UM) model, the twist is initially implanted in a current-carrying bundle of magnetic field lines which then gradually shrinks. Since crustal heating is caused by back-flowing currents in the j-bundle, a decrease in the size of the j-bundle also implies a decrease in the heated surface area (Beloborodov 2009). We also note that the presence of a negative $\ddot{\rm P}$, as follows from our timing analysis, is in agreement with the UM. In fact, immediately prior to the outburst, when the magnetic field of the star is expected to be highly twisted, the star is subject to a large amount of spin-down torque and therefore the spin-down rate is larger with respect to its value in quiescence. If, later during the decay, the field untwists, then the spin-down rate should return to the (secular) pre-outburst value. Therefore in this phase a negative second derivative of the spin period should be observed.

To further test the possibility that a surface zone heated by the j-bundle currents is visible at certain phase intervals, we calculated the BB emission area and the luminosity corresponding to the hot and warm components observed in the four phase segments. A simple UM model predicts a relation between the luminosity L and the emitting area A of the form $L \propto A^2$ (see Beloborodov 2009). By assuming $L \propto A^n$, for the warm component we found a PL index of $n = 1.6$, 1.0, 0.7, 0.9 in the phase interval P1, P2, P3 and P4, respectively. The correspondent index relative to the hot component are $n = 1.4$, 2.3, 1.9, 1.0. Therefore only some of the measured relations are close to the theoretical expectations. As an example, in Figs 13 and 14 we show the evolution of the luminosity with respect to the emitting area as observed for the warm component during phase intervals P3 and P1, respectively (the dashed lines represent the relation expected theoretically). As it can be seen, the evolution observed during P1 is compatible with being related to an evolving current-carrying bundle, while the warm component observed during P3, which evolves very differently ($L \propto A^{0.7}$), may be related to a different emission mechanism. The luminosity/area relation detected at P3 is much flatter, and seems to become steeper and steeper as the outburst decay progresses. Our fitting model, which does not allow us to reconstruct the location of these components on the star surface, is however too simplicistic to derive more robust conclusions.

A particular case is the evolution of the warm temperature relative to the P3 phase interval (Fig. 9, upper panel), which remains (within the 1σ errors) constant up to the second to last observation. Then in the last observation, the hot BB is not present anymore and the spectrum becomes consistent with a single free BB at ∼0.5 keV besides the fixed BB at 150 eV (and about 5 km of radius). This indicates that in this phase interval at later times only the warm region survives, possibly engulfing the hotter spot. Or, it can be interpreted in terms of the warm BB being slowly heated by the hotter region (hot BB), which dissipates (or shrinks out of the line of sight) as a result.

Fig. 1 shows the flux evolution of the SWIFT J1822.3−1606 during the outburst decay. If we assume the peak luminosity to be of a few 10^{35} erg s^{-1}, as inferred by R12 based on magneto-thermal evolutionary models, it implies a distance to the source of ∼2 kpc. This is consistent with the distance to the Galactic H II region M17, described in Section 2.2; and provides further support for the $N_{\rm H}$ and distance values assumed in this work.

We also reported the detection of a phase and energy-variable spectral line (Figs 10 and 11). As it can be seen in Fig. 10, a dark V-shaped feature is visible in the *RXTE* data at phases ∼0.9–1.1, followed by a dark area around phases 1.2–1.3. The energy of the feature varies between ∼5 and ∼12 keV. There is also another feature at lower energy (∼2 keV) at phase ∼0.5, which, if significant, may be just a continuation of the main feature (this is supported by the line width evolution but not by the line energy evolution, see the two upper panels of Fig. 11). A similar phase and energy dependent feature has been detected so far only in two sources: the low-B magnetar SGR 0418 (see T13) and the X-ray dim isolated NS RX J0720.4−3125 (see Borghese et al. 2015). As in these sources the feature may be due to proton–cyclotron resonant scattering of X-ray photons emitted by the star surface on to charges flowing in a small coronal magnetic loop (for alternative interpretations see the discussion in T13 and Borghese et al. 2015). The energy variation of the line would be caused by magnetic field gradients along the coronal loop: as the NS rotates, photons directed towards us intercept sections of the loop with different magnetic field intensities. In the rest frame of the emitters, the proton–cyclotron energy is $E_{\mathrm{cp}} = \hbar eB/m_{\mathrm{p}}c \approx 0.63B_{14}$ keV, where $B_{14} = B/(10^{14}\mathrm{G})$. Assuming that the line is emitted near the surface of the star, its energy as measured by a distant observer is significantly affected by gravitational redshift. Thus, the magnetic field in the small corona loop can be estimated as $B_{14} = (1+z)E_{\mathrm{obs}}/0.63$ keV, where E_{obs} is the observed energy of the line, and $z = 2GM_{\mathrm{NS}}/R_{\mathrm{NS}}c^2 \approx 0.35$ (using an NS mass of $M_{\mathrm{NS}} \approx 1.4\,\mathrm{M}_{\odot}$) and a radius of $R_{\mathrm{NS}} \approx 10$ km). In the case of SWIFT J1822.3−1606 (E_{obs} between 3 and 12 keV) the resulting magnetic field in the coronal loop is in the (6–25) × 10^{14} G range.

We note that the absorption line centroids, as inferred from the *RXTE* PCA, are predominantly at energies close to the upper bound of both the *XMM–Newton* and *Chandra* spectral ranges, or even higher (Fig. 11, upper panel). Therefore, due to the steep spectrum of SWIFT J1822.3−1606 and the rapid decrease of the response of these instruments at energies above about 6 keV, translating into small count statistics, this feature becomes undetectable. In fact, it would be virtually indistinguishable from a modification of a broad spectral component (such as the hot BB) when observed in the *XMM–Newton* or *Chandra* spectral range.

In the case of SGR 0418+5729 instead, the line phase variability could be better characterized because the line centroid energy extended down to ∼1 keV, where the *XMM–Newton* effective area has its maximum. Moreover, the effect of cyclotron scattering by currents in a magnetic loop is more pronounced when most of the X-ray radiation is produced by a single hotspot on the magnetar surface, as in SGR 0418+5729 rather than by two different regions, as in SWIFT J1822.3−1606.

The discovery of a second magnetar with a magnetic field in the radio-pulsar range strengthens the idea that magnetars are much more common than expected so far. Dormant magnetars may lurk among unidentified, weak X-ray sources and reveal themselves only when they enter an outburst phase. The detection of phase-variable absorption lines in the spectra of both the low-field magnetars discovered up to now is remarkable, the more given that a similar feature has been observed only in the thermally emitting NS RX J0720.4−3125, which has a comparable dipole field but has not exhibited any magnetar-like behaviour. Whether this is a further proof of a (much suspected) link between magnetars and the seven thermally emitting isolated NSs is still an open issue.

ACKNOWLEDGEMENTS

We acknowledge the use of public data from the *Swift*, *XMM–Newton* and *Chandra* data archives. PE acknowledges a Fulbright Research Scholar grant administered by the US–Italy Fulbright Commission and is grateful to the Harvard–Smithsonian Center for Astrophysics for hosting him during his Fulbright exchange.

REFERENCES

Albano A., Turolla R., Israel G. L., Zane S., Nobili L., Stella L., 2010, ApJ, 722, 788
Anders E., Grevesse N., 1989, Geochim. Cosmochim. Acta, 53, 197
Asplund M., Grevesse N., Sauval A. J., Scott P., 2009, ARA&A, 47, 481
Balucinska-Church M., McCammon D., 1992, ApJ, 400, 699
Beloborodov A. M., 2009, ApJ, 703, 1044
Borghese A., Rea N., Coti Zelati F., Tiengo A., Turolla R., 2015, ApJ, 807, L20
Cummings J. R., Burrows D., Campana S., Kennea J. A., Krimm H. A., Palmer D. M., Sakamoto T., Zan S., 2011, Astron. Telegram, #3488
Duncan R. C., Thompson C., 1992, ApJ, 392, L9
Feldman U., 1992, Phys. Scr., 46, 202
Gotthelf E. V., Halpern J. P., Buxton M., Bailyn C., 2004, ApJ, 605, 368
Ibrahim A. I. et al., 2004, ApJ, 609, L21
Lodders K., 2003, ApJ, 591, 1220
Makishima K. et al., 1990, ApJL, 365, L59
Mereghetti S., 2008, Astron. Astrophys. Rev., 15, 225
Nielbock M., Chini R., Jütte M., Manthey E., 2001, A&A, 377, 273
Pagani C., Beardmore A. P., Kennea J. A., 2011, Astron. Telegram, #3493
Perna R., Pons J. A., 2011, ApJ, 727, L51
Protassov R., van Dyk D. A., Connors A., Kashyap V. L., Siemiginowska A., 2002, ApJ, 571, 545
Rea N., Esposito P., 2011, in Rea N., Torres D. F., eds, Astrophysics and Space Science Proceedings, High-Energy Emission from Pulsars and their Systems. Springer, Berlin, p. 247
Rea N. et al., 2012, ApJ, 754, 27 (R12)?
Rea N. et al., 2013, ApJ, 770, 65
Rea N., Viganò D., Israel G. L., Pons J. A., Torres D. F., 2014, ApJ, 781, L17
Rodríguez Castillo G. A., Israel G. L., Esposito P., Pons A., Turolla R., Viganò D., Zane S., 2014, MNRAS, 441, 1305
Scholz P., Ng C.-Y., Livingstone M. A., Kaspi V. M., Cumming A., Archibald R. F., 2012, ApJ, 761, 66
Scholz P., Kaspi V. M., Cumming A., 2014, ApJ, 786, 62
Thompson C., Duncan R. C., 1995, MNRAS, 275, 255
Tiengo A. et al., 2013, Nature, 500, 312 (T13)
Townsley L. K., Feigelson E. D., Montmerle T., Broos P. S., Chu Y.-h., Garmire G. P., 2003, ApJ, 593, 874
Turolla R., Zane S., Pons J. A., Esposito P., Rea N., 2011, ApJ, 740, 105
Wilms J., Allen A., McCray R., 2000, ApJ, 542, 914
Zhou P., Chen Y., Li X.-D., Safi-Harb S., Mendez M., Terada Y., Sun W., Ge M.-Y., 2014, ApJ, 781, L16

This paper has been typeset from a TEX/LATEX file prepared by the author.